

Research Article

The Research on Second-Order ADRC Algorithm of Using Wind Turbine Virtual Inertia to Participate in Primary Frequency Regulation in a Small Stand-Alone Microgrid

Wang Yi ¹, Jiang Hanhong¹ and Xing Pengxiang²

¹National Key Laboratory of Science and Technology on Vessel Integrated Power System, Naval University of Engineering, Wuhan 430033, China

²School of Electrical Engineering, Wuhan University, Wuhan 430072, China

Correspondence should be addressed to Wang Yi; wangyi500500@163.com

Received 19 August 2017; Accepted 31 October 2017; Published 15 March 2018

Academic Editor: Ton D. Do

Copyright © 2018 Wang Yi et al. This is an open access article distributed under the Creative Commons Attribution License, which permits unrestricted use, distribution, and reproduction in any medium, provided the original work is properly cited.

In order to improve the transient stability of frequency in a small stand-alone microgrid (SSM), this paper takes a SSM composed of a direct-drive permanent magnet synchronous generator (D-PMSG) and a micro gas turbine (MGT) as the background and uses wind turbine generator (WTG) virtual inertia (VI) to participate in the primary (short-term) system frequency regulation. First of all, this paper constructs a grid-connected model composed of a WTG and a MGT, analyzes the WTG virtual inertia frequency regulation mechanism, and explains the principle of proportional-differentiation (PD) virtual inertia control (VIC) and its shortcomings. Secondly, the paper introduces the structure principle of n -order active disturbance rejection control (ADRC) and deduces the design process of second-order ADRC-VIC. Finally, through the simulation and experimental verification, comparing the frequency perturbation of without-VIC, PD-VIC, and ADRC-VIC, it is concluded that PD-VIC and ADRC-VIC both can use the WTG virtual inertia to participate in the primary frequency regulation. The frequency regulation effect of ADRC-VIC is better than PD-VIC, ADRC-VIC can extend the rotor speed recovery time and avoid overshoot, and its frequency fluctuation amplitude and settling time are obviously improved, and ADRC-VIC can effectively avoid the overshoot phenomenon of the MGT output power.

1. Introduction

The small stand-alone microgrid (SSM) is an effective way to solve the power supply in the mountains, islands, and remote areas. The principle is to use the collected wind energy, solar energy, and other renewable energy to connect with the traditional synchronous generator (SG), thus building a power supply system independent of the large power grid [1–3]. With the progress of wind power technology, its application in the stand-alone microgrid is more and more extensive. Direct-drive permanent magnet synchronous generator (D-PMSG) has the advantages of flexible control, good reliability, and high power generation efficiency, and it has good application prospect [4]. Micro gas turbine (MGT) has the advantages of low emissions, high efficiency, good fuel adaptability, and flexible control, and it is widely used in distributed power generation technology [5].

In this paper, a SSM constructed by a D-PMSG and MGT is used as the research object to analyze the problem of the transient stability of frequency. The master-control power supply of the SSM is MGT, so the stability of frequency mainly relies on MGT. On the one hand, due to economic reasons, the design capacity of microgrid and the demand of load are matched, resulting in the fact that the microgrid capacity is limited and the system inertia is small. On the other hand, due to technical reasons, the system inertia can only damp the system frequency changes, but it can not completely prevent the system frequency changes [6–8]. Therefore, the system requires the WTG to actively participate in the frequency response, so as to improve the transient stability of system frequency. In general, WTG participates in system frequency regulation in two ways [9–11]. One is called deloaded operation of WTG; when the system frequency has a deviation,

the WTG releases the standby power to participate in the system frequency regulation. This process takes a long time, but it is at the expense of wind energy utilization and the operating economy of WTG, and it is difficult to promote the application. The other is virtual inertia control (VIC) [12]; since the WTG itself has mechanical inertia, it has available rotor kinetic energy in operation. The rotor kinetic energy can transform into electromagnetic power through the control algorithm, to provide support for the system frequency, and this process takes a short time and “zero power consumption” [13, 14]. In addition, the permeability of wind power is often larger due to the limited capacity of SSM, which ensures the effectiveness of WTG participating in the system transient frequency regulation [15–17]. Many scholars have started the research on how to use the virtual inertia of WTG in the system frequency regulation and improve the transient stability of frequency.

The paper [12] gives smart microgrid hierarchical frequency control ancillary service provision based on virtual inertia concept, both the static and dynamic frequency securities of an islanded microgrid are provided in primary and secondary control levels. In [10, 11], frequency-based VIC is realized based on the rate of change of frequency (ROCOF) df/dt or frequency deviation Δf from the nominal value or a combination of both. The proportional (P) term with Δf makes the WTG respond to frequency changes and the differential (D) term with df/dt emulates the inertia. The paper [13] introduces a method of PD-VIC to improve the primary frequency contribution of grid-connected variable speed WTG; by adjusting the droop of the WTG in response to wind velocities, the system primary frequency response is significantly improved. In [14], it is concluded that WTG can provide an extra active power production from its stored kinetic energy; the amount of extra injected power is determined according to the frequency deviation Δf and/or the rate of change of frequency df/dt .

The above literatures illustrate the feasibility of using virtual inertia to participate in system frequency regulation and PD-VIC has a certain practicality. However, the PD algorithm has its inherent limitations, such as the fact that it is difficult to determine the optimal control parameters and likely to cause an overshoot, and the robustness of the controller is poor.

This paper attempts to design a controller from the view of suppressing the system frequency disturbance, which has strong robustness and can avoid overshoot. In [18], the performance superiority of WTG with the proposed linear ADRC approach over that with the traditional proportional integral and fuzzy-proportional integral-based controllers is validated by the simulation results. The simulation results indicate that the performance of the LADRC-based controller is much better than PI and Fuzzy-PI-based controllers. The result also shows that the proposed LADRC-based controller has an excellent robustness and a good capability of disturbance rejection. The authors of [19, 20] have presented the ADRC for the doubly fed induction generator (DFIG) used in wind energy conversion systems, the proposed control has demonstrated its effectiveness under wind variation, and both generated power and rotational speed are kept in their safety region.

Based on the above research, this paper studies the PD-VIC and second-order ADRC-VIC algorithms, and it analyzes the frequency regulation mechanism of the two algorithms. Under the premise of not exceeding WTG virtual inertia frequency regulation capability, the characteristics of the two algorithms are compared and analyzed by simulation and experiment.

The remainder of this paper is given as follows. Section 2 gives a single WTG grid-connected structure and the mechanism of VIC. In Section 3, the structure of n -order ADRC is described first, and then the second-order ADRC is designed according to the frequency dynamic response equation. Simulation analysis and experiment verification are given in Sections 4 and 5, respectively. Finally, conclusions are drawn in Section 6.

2. A WTG Grid-Connected Structure and the Mechanism of VIC

2.1. A WTG Grid-Connected Structure. After a WTG combined to the grid, the system structure is shown in Figure 1. The WTG includes wind wheel, D-PMSG, full-power converter, and its control system.

The wind turbine (WT) is used to capture the wind energy through the wind wheel to drive the D-PMSG to generate electricity. The motion equation of the WTG rotor is

$$2H_w \frac{d\omega_w}{dt} = P_{\text{wind}} - P_w, \quad (1)$$

where H_w denotes the inertia time constant of D-PMSG, ω_w the rotor speed of wind wheel, P_{wind} the mechanical power captured by wind turbine, and P_w the electromagnetic power of the WTG.

The expression of P_{wind} is [21]

$$P_{\text{wind}} = 0.5\rho\pi R^2 v^3 C_p(\lambda, \theta), \quad (2)$$

where ρ denotes the air density, R the radius of the wind wheel, v the wind speed, $C_p(\lambda, \theta)$ the power coefficient of WTG, θ the pitch angle, and λ the tip speed ratio. The expression of $C_p(\lambda, \theta)$ is as follows:

$$C_p(\lambda, \theta) = 0.22 \left(\frac{116}{\sigma} - 0.4\theta - 5 \right) e^{(-12.5/\sigma)} \quad (3)$$

$$\sigma = \frac{1}{(1/(\lambda + 0.08\theta) - 0.035/(\theta^3 + 1))}$$

$$\lambda = \frac{\omega_w R}{v}.$$

When the pitch angle θ is constant, $C_p(\lambda, \theta)$ is a function of λ . $C_p(\lambda, \theta)$ can reach the maximum value $C_{p\text{max}}(\lambda, \theta)$ by adjusting the rotor speed ω_w and λ reaches the optimal value λ_{opt} at the same time, as shown in Figure 2(a). At this point, it can be seen from (2) that P_{wind} corresponds to only one maximum point ($P_{\text{max}}, \omega_{\text{wopt}}$) at different wind speeds v and rotor speed ω_w , and these maximum points are connected to a line, which is the maximum power point tracking (MPPT) curve, as shown in Figure 2(b).

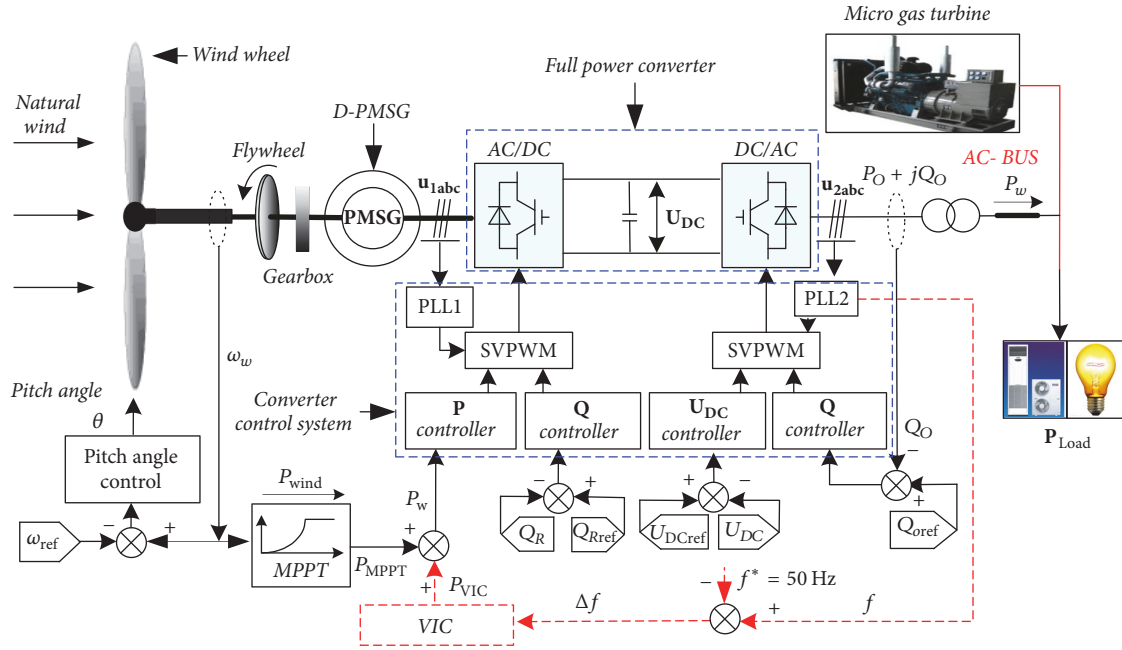


FIGURE 1: A wind turbine system structure after the grid-connection.

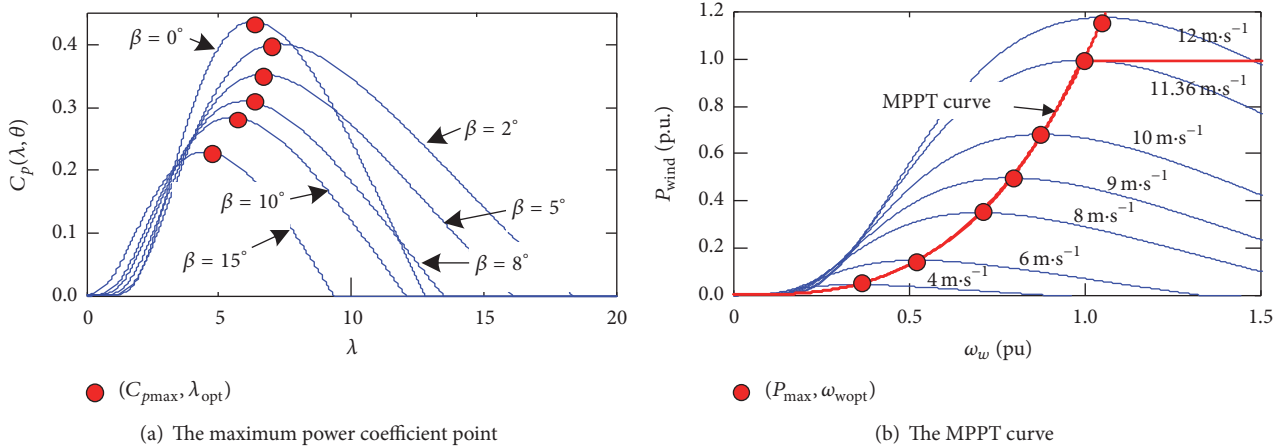


FIGURE 2: The MPPT control of WTG.

When the WTG runs according to the MPPT curve, the wind energy obtained by WTG is

$$P_{\text{MPPT}} = k_{\text{max}} \omega_w^3, \quad (4)$$

where k_{max} is the coefficient that makes WTG obtain the maximum wind energy, and its expression is $k_{\text{max}} = 0.5\rho\pi R^5 C_{p\text{max}}(\lambda, \theta) / \lambda_{\text{opt}}^3$. When the VIC is introduced into the microgrid, as shown by the red dotted line in Figure 1, the expression of P_w is

$$P_w = P_{\text{MPPT}} + P_{\text{VIC}}, \quad (5)$$

where P_{MPPT} is the output power of the MPPT control and P_{VIC} is the auxiliary frequency regulation power of VIC output. As shown in Figure 1, the input of VIC is the system

frequency deviation Δf , and $\Delta f = f - f^*$, f is the system frequency obtained by the grid-side phase-locked loop (PLL), and f^* is the reference frequency 50 Hz. P_{VIC} is calculated by the frequency deviation Δf . When the system is in steady-state operation, that is, $|\Delta f| = 0$, $P_{\text{VIC}} = 0$, the WTG runs in the state of MPPT control, and virtual inertia does not participate in the system frequency regulation. When the system frequency is disturbed, that is, $|\Delta f| > 0$, $P_{\text{VIC}} \neq 0$, the WTG adjust the generator rotating speed and output power through the full-power converter to use virtual inertia in the system frequency regulation.

2.2. The Response Mechanism of VIC. The operation process of WTG includes MPPT and VIC. Figure 3 shows the characteristic curves of WTG in the processes of MPPT and VIC.

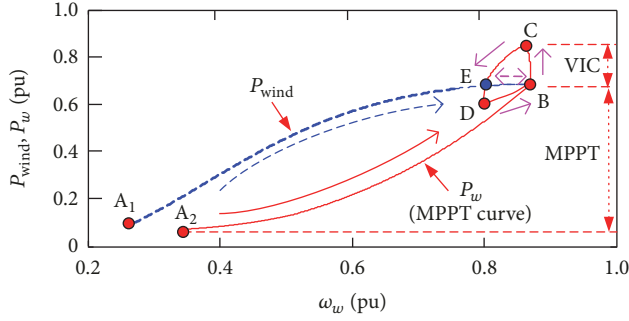


FIGURE 3: The WTG response processes of MPPT and VIC.

The wind speed v keeps constant $7 \text{ m}\cdot\text{s}^{-1}$, and the system load is increased by 15% after WTG reached the MPPT point (B). P_{wind} and P_w denote the mechanical power and the electromagnetic power, respectively.

The Process of MPPT ($A_i \rightarrow B$). The process by which WTG changes from point A_i ($i = 1, 2$) to point B is the MPPT process under the constant wind speed. In this process, P_w changes along the curve of MPPT, and P_{wind} of WTG changes along its characteristic curve. As P_{wind} is greater than P_w , ω_w is constantly rising, and the system is stable at point B ultimately. As can be seen from the curve of P_w in Figure 3, point B is the maximum power point of WTG at this wind speed.

The Process of VIC ($B \rightarrow C \rightarrow D \rightarrow B$). When the system frequency falls due to the sudden increase in load, the VIC of WTG makes P_w climb from points B to C quickly. In this process, due to the inertia of WTG, ω_w does not change immediately, so P_{wind} remains at point B. At this time, since P_{wind} is less than P_w , ω_w starts to decrease. During the decrease process of ω_w , P_{wind} changes along the curve $B \rightarrow E$, and P_w runs along the curve $C \rightarrow D$, when the system finally runs to point D, and then ω_w reaches the minimum value. At this time, P_{wind} is greater than P_w , ω_w starts to increase, P_{wind} of WTG change along the curve $E \rightarrow B$, P_w run along the curve $D \rightarrow B$, the system is back to point B finally, the mechanical power P_{wind} and the electromagnetic power P_w are balanced again, and the rotor speed ω_w is stabilized at the optimal speed of point B.

In the process of VIC, the principle of auxiliary frequency regulation is mainly to change the power of WTG to reduce the impact of the system load disturbance on the MGT, thereby reducing the changing rate and amplitude of the system frequency.

2.3. The Rotor Speed Recovery and Overshoot. As shown in Figure 4, when the system frequency drops, VIC can quickly reduce the rotor speed and release the rotor kinetic energy. WTG delivers active power to the system for a short period of time to provide support for the system frequency. The inherent drawback of this process is that, at the rapid recovery of the rotor speed, on the one hand, this causes the oscillation and overshoot phenomenon of the WTG output power and

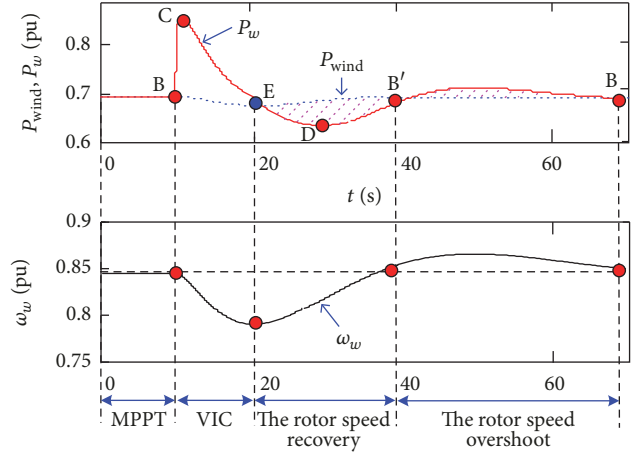


FIGURE 4: The recovery and overshoot of the rotor speed.

the rotor speed (the shadow portion of the $E \rightarrow B$ time period); on the other hand, during the rotor speed recovery process, the WTG absorbs energy from the grid (the shadow portion of the $E \rightarrow B'$ time period), resulting in a smaller power supply to the microgrid, which is not conducive to frequency recovery stability.

In fact, the rotor speed recovery process is carried out when the frequency is not stable, this process is to reduce the WTG output power and increase the system load, which has played a “superposition effect” in the decline process of the frequency, making the frequency response characteristics deteriorate, and in severe cases can cause the system frequency to fall twice.

In Figure 4, $B \rightarrow E$ is the time period of VIC. $E \rightarrow B$ is the time period of the rotor speed recovery and overshoot, which is the time of the rapid decline in frequency regulation capacity, through extending this time period to slow down the speed recovery rate, so as to reduce the rapid decline of frequency regulation capacity and reduce the system frequency deviation.

3. Second-Order ADRC-VIC

ADRC is proposed by Han [22], which is based on the error feedback control theory of traditional PID and the development of modern control theory [23, 24]. ADRC is less dependent on the accuracy of the mathematical model of the controlled object, and the main idea is to estimate the system real-time disturbance by using the extended state observer (ESO) [25] and compensate it. ADRC has the characteristics of fast response, robustness, and adaptability [26]. In this paper, the second-order ADRC is designed according to the frequency dynamic response equation of the microgrid.

MGT is the main control power supply, which can be equivalent to conventional synchronous generator model for analysis, and the system voltage fluctuations caused by the load switching will not be taken into account. Thus, the constant E'_q of the synchronous generator model (in p.u.) is as follows:

$$\begin{aligned} u_d &= x_q i_q - r_s i_d \\ u_q &= E'_q - x'_d i_d - r_s i_q \end{aligned} \quad (6)$$

$$2H\dot{\omega} = T_m - E'_q i_q + (x'_d - x_q) i_d i_q - D\omega,$$

where u_d , u_q , i_d , and i_q are d -axis voltage, q -axis voltage, d -axis current, and q -axis current of the generator, respectively. x'_d and x_q are the d -axis transient reactance and q -axis reactance, respectively. r_s denotes the stator resistance. ω is the rotor speed. H and D are the rotational inertia and the damping coefficient, respectively. T_m is the mechanical torque.

Laplace transformation of (7) can be expressed as

$$\begin{aligned} u_d &= x_q i_q - r_s i_d \\ u_q &= E'_q - x'_d i_d - r_s i_q \\ 2Hs\omega &= T_m - E'_q i_q + (x'_d - x_q) i_d i_q - D\omega. \end{aligned} \quad (7)$$

The speed governor model of the synchronous generator can be expressed as

$$\begin{aligned} T_m &= k_1 \Delta\omega + k_2 \frac{\Delta\omega}{s} \\ \Delta\omega &= \omega_{\text{ref}} - \omega, \end{aligned} \quad (8)$$

where k_1 and k_2 are the proportional and integral coefficients of PI controller, respectively. ω_{ref} is the reference value of the synchronous generator speed. The active power P_{MGT} of the microgrid synchronous generator can be expressed as

$$P_{\text{MGT}} = u_d i_d + u_q i_q. \quad (9)$$

Substituting (8), (9), and $i^2 = i_d^2 + i_q^2$ into (8) leads to

$$P_{\text{MGT}} = k_1 \Delta\omega + k_2 \frac{\Delta\omega}{s} - D\omega - 2Hs\omega - r_s i^2. \quad (10)$$

It is known from (10) that the VIC system frequency response dynamic equation is

$$2Hs\Delta f = P_{\text{MPPT}} + P_{\text{MGT}} - P_L - D\Delta f + P_{\text{VIC}}. \quad (11)$$

Substituting (10) into (11) leads to

$$\begin{aligned} 2Hs\Delta f + D\Delta f &= k_1 \Delta\omega + k_2 \frac{\Delta\omega}{s} - D\omega - 2Hs\omega + P_A \\ &+ P_{\text{VIC}}, \end{aligned} \quad (12)$$

where $P_A = P_{\text{MPPT}} - P_L - r_s i^2$.

The relationship between the system frequency (p.u.) and the generator rotor speed (p.u.) is expressed as

$$\begin{aligned} f &= \omega \\ \Delta f &= \Delta\omega. \end{aligned} \quad (13)$$

Substituting (13) into (12) leads to

$$\begin{aligned} (2Hs + D)\Delta f &= \left(k_1 + \frac{k_2}{s}\right)\Delta f - (D + 2Hs)f + P_A \\ &+ P_{\text{VIC}}. \end{aligned} \quad (14)$$

Both sides of the equation are multiplied by s , and then

$$\begin{aligned} (2Hs^2 + Ds - k_1s + k_2)\Delta f \\ = -(D + 2Hs)sf + s(P_A + P_{\text{VIC}}). \end{aligned} \quad (15)$$

Namely,

$$\begin{aligned} 2H\Delta\ddot{f} + (D - k_1)\Delta\dot{f} + k_2\Delta f \\ = -D\dot{f} - 2H\ddot{f} + \dot{P}_A + \dot{P}_{\text{VIC}}. \end{aligned} \quad (16)$$

Substituting $\dot{f} = \Delta\dot{f}$ into (16) leads to

$$4H\Delta\ddot{f} + (2D - k_1)\Delta\dot{f} + k_2\Delta f = \dot{P}_A + \dot{P}_{\text{VIC}}. \quad (17)$$

The second-order differential equation of the power system frequency deviation Δf is expressed as

$$\Delta\ddot{f} = \frac{1}{4H} \left((k_1 - 2D)\Delta\dot{f} - k_2\Delta f + \dot{P}_A \right) + \frac{\dot{P}_{\text{VIC}}}{4H}, \quad (18)$$

where the uncertain items of the controlled object can be defined as the sum of internal and external disturbance as follows:

$$\begin{aligned} f(x_1, x_2, t, w(t)) \\ = \frac{1}{4H} \left((k_1 - 2D)\Delta\dot{f} - k_2\Delta f - \dot{P}_A \right). \end{aligned} \quad (19)$$

The differential equation of Δf and P_{VIC} in (18) indicates that when the ADRC is substituted for the conventional PD controller, the output of the controlled object is the same as that of the conventional PD controller, which is the value of the system frequency deviation Δf . The block diagram of the second-order ADRC is based on (18), as shown in Figure 5.

In Figure 5, z_1 is the estimated value of the system frequency deviation value Δf , z_2 is the estimated value of $\Delta\dot{f}$, and z_3 is the estimated value of the system uncertain item $(1/4H) * ((k_1 - 2D)\Delta\dot{f} - k_2\Delta f + \dot{P}_A)$. a denotes the compensation coefficient of the estimated values z_3 and z_2 . In this paper, $a = 4H$ and $b = 1/4H$. Since the purpose of the ADRC is to suppress fluctuations in system frequency, the reference values Δf^* and $\Delta\dot{f}^*$ of variation in status can be directly set to 0, respectively. Thus, the design of TD shown in Figure 5 is left out.

In practical engineering applications, there is a need to discretize the algorithm of each module for the ADRC [22, 23]. The discretized form of the nonlinear ESO can be expressed as

$$\begin{aligned} e(k) &= z_1(k) - x_1(k) \\ z_1(k+1) &= z_1(k) + h(z_2(k) - \beta_1 e(k)) \\ z_2(k+1) &= z_2(k) + h(z_3(k) - \beta_2 \text{fal}(e(k), \alpha_1, h) + bu(k)) \\ z_3(k+1) &= z_3(k) + h(-\beta_3 \text{fal}(e(k), \alpha_2, h)), \end{aligned} \quad (20)$$

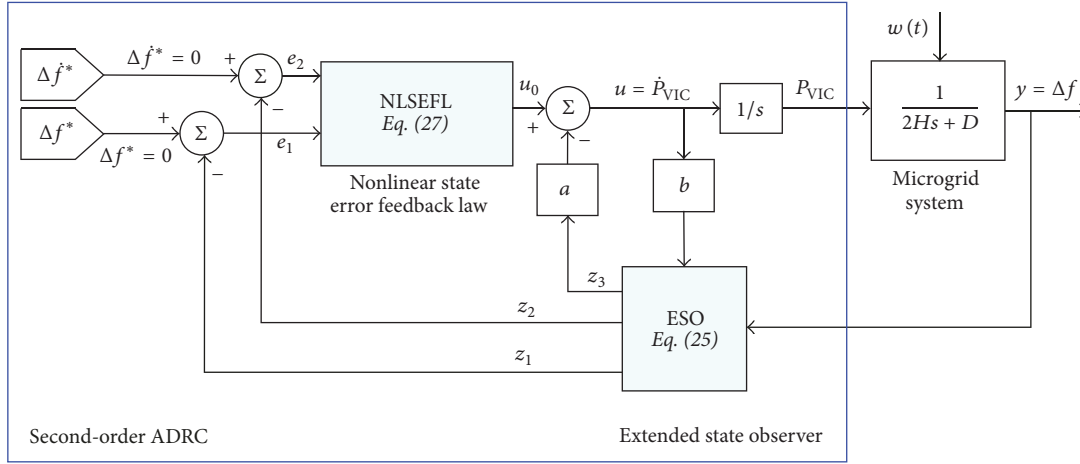


FIGURE 5: Diagram of second-order ADRC controller.

where h is the sampling step size and β_1, β_2 , and β_3 are the observer parameters needed to be determined. According to the characteristics of inherent parameters of the ADRC, $\beta_1 = 1/h$, $\beta_2 = 1/3h^2$, and $\beta_3 = 1/32h^3$, which are used in this paper. In order to avoid the chattering, the saturation function $\text{fal}(e, a, \delta)$ is expressed as

$$\text{fal}(e, a, \delta) = \begin{cases} \frac{e}{\delta^{\alpha-1}} & |e| \leq \delta \\ |e|^\alpha \text{sgn}(e) & |e| > \delta, \end{cases} \quad (21)$$

where δ is the linear interval length and $\text{sgn}(\cdot)$ is the symbolic function and a denotes the saturation function factor. When the absolute value of the error e is relatively large, its gain will decrease to prevent the overshoot. When the absolute value of the error e is relatively small, its gain will increase to speed up the convergence process.

The NLSEF and the discrete control amount produced by disturbance compensation are expressed as

$$\begin{aligned} e_1(k) &= \Delta f^* - z_1(k) \\ e_2(k) &= \Delta \dot{f}^* - z_2(k) \\ u_0(k) &= \beta_{01} \text{fal}(e_1(k), a_{01}, \delta_0) \\ &\quad + \beta_{02} \text{fal}(e_2(k), a_{02}, \delta_0) \\ u(k) &= u_0(k) - az_3(k), \end{aligned} \quad (22)$$

where β_{01} and β_{02} are the output correction coefficients and the parameters $0 < a_{01} < 1 < a_{02}$ are used to mediate the nonlinearity of the $\text{fal}(e, a, \delta)$ function. The ADRC designed in this paper has the following advantages over the conventional PD controller: (1) due to its observation and compensation of power disturbance, its better dynamic characteristic of suppressing the frequency disturbance; (2) increasing the error tracking efficiency by designing the optimized NLSEF and using saturation function to achieve the objective of “small error and large gain, large error and small gain”; (3) its better applicability and robustness because of adopting ESO

for the estimation and compensation of the system parameter disturbance.

Although the parameters of ADRC are much more than PD, the advantages of ADRC over PD are as follows. On the one hand, in order to release more WTG virtual inertia, the PD is achieved by increasing the proportional factor k_p and differential factor k_d , but this causes the WTG speed overshoot phenomenon, when the overshoot is serious which will cause the system frequency secondary drop. On the other hand, as more WTG virtual inertia was released, ADRC will not cause the WTG rotor speed overshoot, and its ability to adjust the system frequency will be further improved. And ADRC has a certain ability to resist parameter disturbance. The following is through simulation and experiment to illustrate this.

4. Simulation Analysis

In this paper, a SSM simulation model composed of a WGT and a MGT is built in MATLAB/Simulink. The main parameters of the simulation model are shown in Appendix A. First of all, the estimation effect of ESO and the robustness of antiparameter perturbation of ADRC are verified by simulation.

4.1. The Simulation of ESO Observation Effect. Figure 6 shows the estimated effect of ESO when the load $P_{\text{Load}1}$ is switched. The red solid line is the p.u. value of the actual system power perturbation, $\Delta P = f(x_1, x_2, t, w(t)) \times 4H$. The blue dotted line is the ESO estimate value. z_3 is the estimate amount of $f(x_1, x_2, t, w(t))$. It can be seen from the figure that ESO can realize the accurate tracking and estimation of the system load disturbance, which provides a reliable basis for the compensation and suppression of the system frequency disturbance.

During the operation of the system, the inertia time constant H of the system is in the process of change due to the random fluctuation of the wind resource and the load disturbance. Therefore, it is necessary to examine the impact

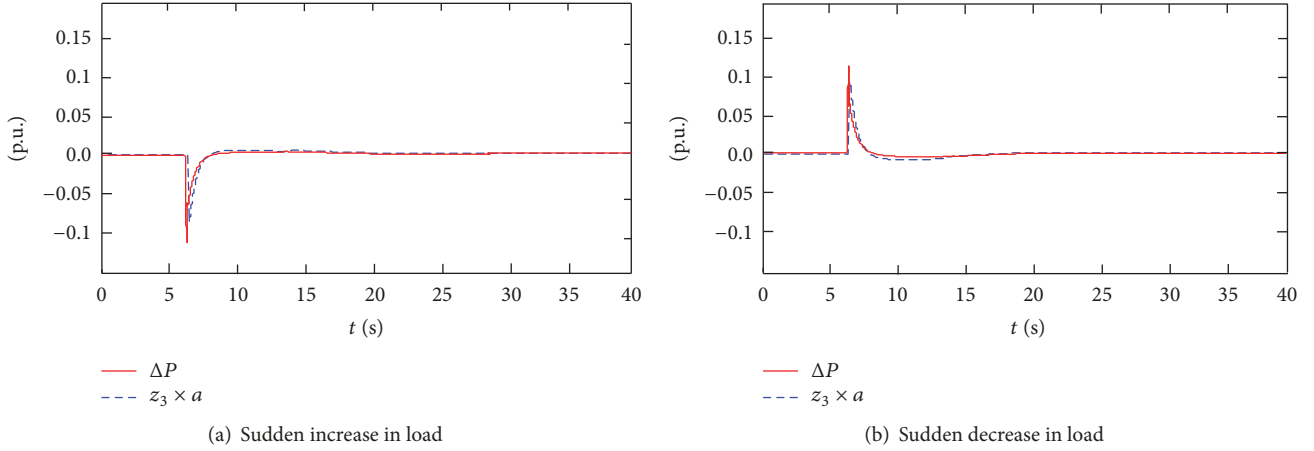


FIGURE 6: Observations of ESO during load switching.

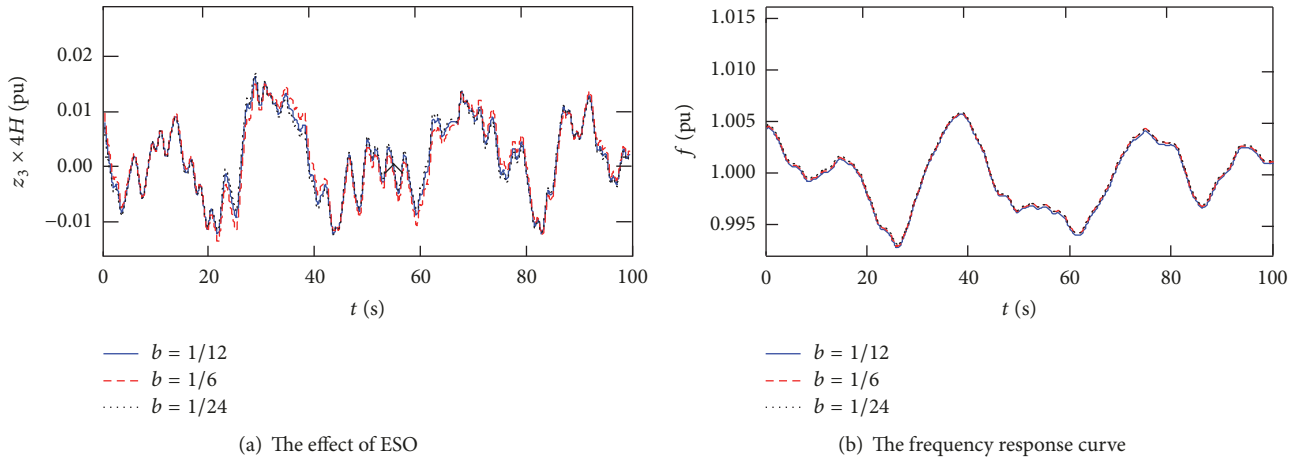


FIGURE 7: The influences of control parameter variation on ADRC performance.

of parameter b on control algorithm performance. When the wind speed fluctuates randomly and b takes $1/12$, $1/6$, or $1/24$, respectively, the ADRC control characteristic is shown in Figure 7.

Figures 7(a) and 7(b) are the estimated effect curves and system frequency response curves of ESO, respectively. As can be seen from Figure 7(b), the frequency response curves of the system are completely coincident with different parameters b . The ESO of ADRC has strong robustness, which is inherent in ESO performance. When the parameter b is disturbed within a certain range, the ADRC control performance is not affected, which is determined by its robustness. Therefore, the change of the value of b will not affect the ESO accurate estimation of the system power disturbance; that is, it will not affect the control effect of ADRC on the system frequency. This shows that ADRC has a certain ability to resist system parameters perturbation, which reduces the ADRC dependence on grid parameters.

4.2. The Simulation of PD-VIC and Second-Order ADRC-VIC. In order to compare the effects of the PD-VIC and second-order ADRC-VIC to suppress the frequency disturbance, the

microgrid frequency disturbance is caused by sudden increase load. Figure 8 is the waveforms of simulation during the sudden increase in load, and wind speed v is 7 m/s.

The design of simulation scenario: at $t = 0$ s, a WTG and MGT are connected to bear the fixed load $P_{load0} = 10$ kW together, the output power of WTG is $P_{WTG} = 3$ kW, the rotor speed of WTG is $\omega_w = 14$ rad/s, and the output power of MGT is $P_{MGT} = 7$ kW. At $t = 5$ s, the sudden increase in load is $P_{load1} = 5$ kW.

In Figure 8, blue dotted lines are without-VIC simulation waveforms. At $t = 5$ s, P_{load1} is put into the system. MGT independently bears the load disturbance, and WTG does not participate in frequency regulation. The frequency nadir is 49.55 Hz and the setting time is at $t = 20$ s after two oscillation periods. $P_{WTG} = 3$ kW and $\omega_w = 14$ rad/s remain unchanged. Since the load disturbance is only borne by MGT, P_{MGT} increases 12 kW by step.

The red long-dotted lines are PD-VIC simulation waveforms. At $t = 5$ s, the WTG uses virtual inertia to participate in frequency regulation. The lowest point f drops to is 49.7 Hz and the setting time is at $t = 18$ s after one oscillation period. During the sudden increase in load, P_{WTG} increases

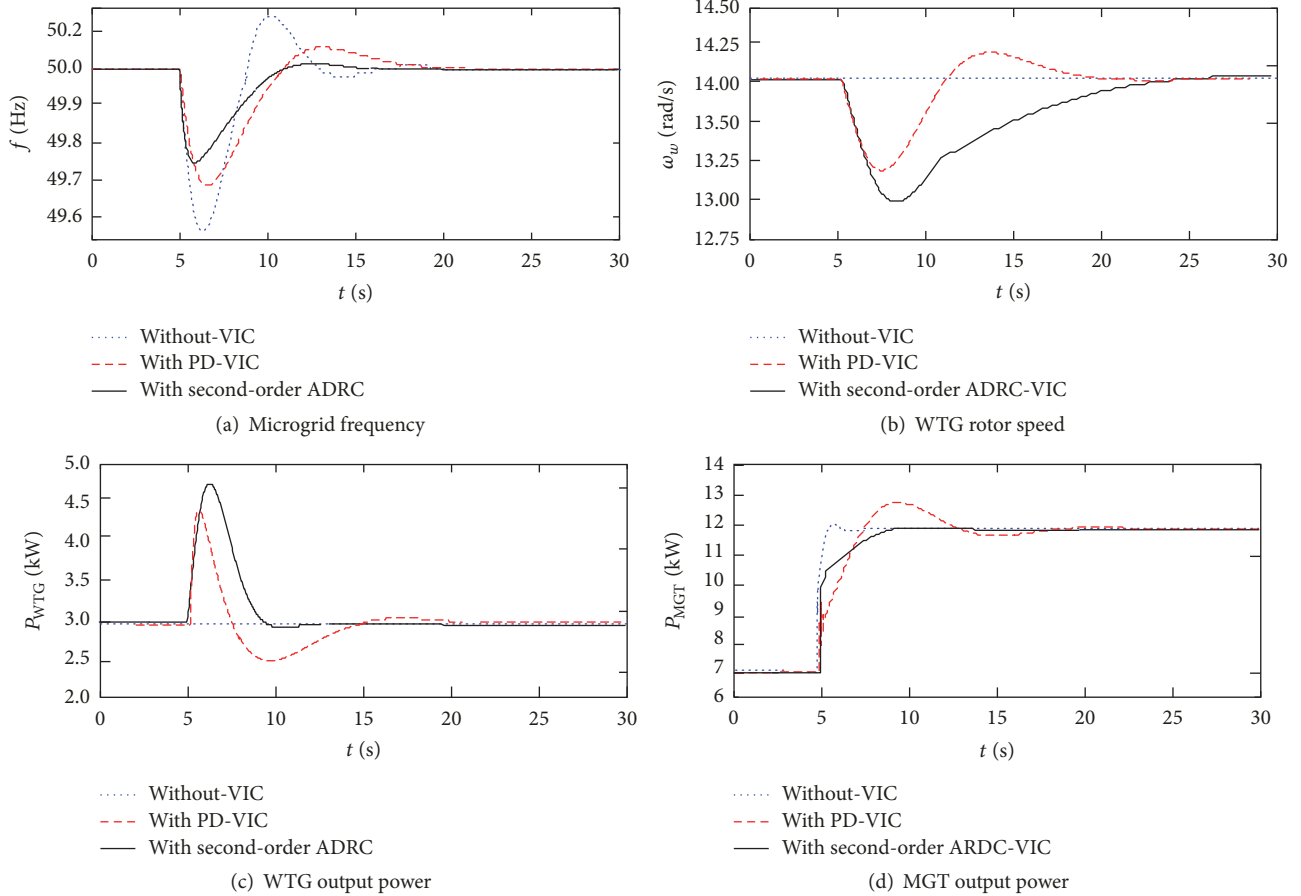


FIGURE 8: The simulation waveforms of sudden increase load.

to the maximum value 4 kW and then returns to 3 kW, ω_w falls to 13.25 rad/s and then returns to 14 rad/s, and P_{WTG} and ω_w have the phenomenon of oscillation and overshoot. P_{MGT} increases to 12 kW after a certain distortion and appears overshoot phenomenon which is higher than 12 kW.

The black solid lines are the second-order ADRC-VIC simulation waveforms. The lowest point f drops to is 49.85 Hz and the setting time is at $t = 16$ s. During the sudden increase in load, P_{WTG} increases to a maximum point 4.5 kW and then returns to 3 kW, ω_w falls to 13 rad/s and then returns to 14 rad/s, and P_{WTG} and ω_w have no phenomenon of oscillation and overshoot. The recovery time of ω_w is longer than PD-VIC. Compared with that in PD-VIC, P_{MGT} does not appear overshoot phenomenon, P_{MGT} can be more smooth added to 12 kW, and second-order ADRC-VIC reduces the impact of load disturbance on MGT.

Based on the above conclusions, when the wind speed is constant, PD-VIC and second-order ADRC-VIC both can use the WTG virtual inertia to participate in the short-term frequency regulation and effectively reduce the transient fluctuations of the system frequency. Compared with PD-VIC, second-order ADRC-VIC can extend the recovery time of ω_w and avoid overshoot, reduce the amplitude of the frequency Δf_{\max} by 0.15 Hz and the settling time Δt by 2 s, and make P_{MGT} more smooth transition during load disturbances.

When the wind speed fluctuates randomly and the system load is constant, the system frequency disturbance is mainly caused by the fluctuation of WTG output power. The effects of different VIC algorithms on suppressing frequency perturbation are compared by simulation in Figure 9. Compared with without-VIC and PD-VIC, second-order ADRC-VIC (blue dash-dotted line) frequency disturbance is significantly smaller. As WTG uses second-order ADRC-VIC to increase the intensity of participating in the frequency regulation, the disturbance range of the rotor speed ω_w becomes larger, which indicates that WTG virtual inertia can be more fully released.

5. Experimental Verification

5.1. The Design of Simulative Experiment Platform. In order to further verify the effectiveness and feasibility of the above algorithms, a set of simulative WTG grid-connected experimental systems with capacity of 275 kVA is built, which includes a simulative WTG and a virtual synchronous generator (VSG) simulated by a full-power converter. The full-power converter simulates the MGT frequency characteristics according to the algorithm in [27]. Figures 10 and 11 are the schematic diagram of the simulative experiment system and the field of the simulative experimental platform, respectively.

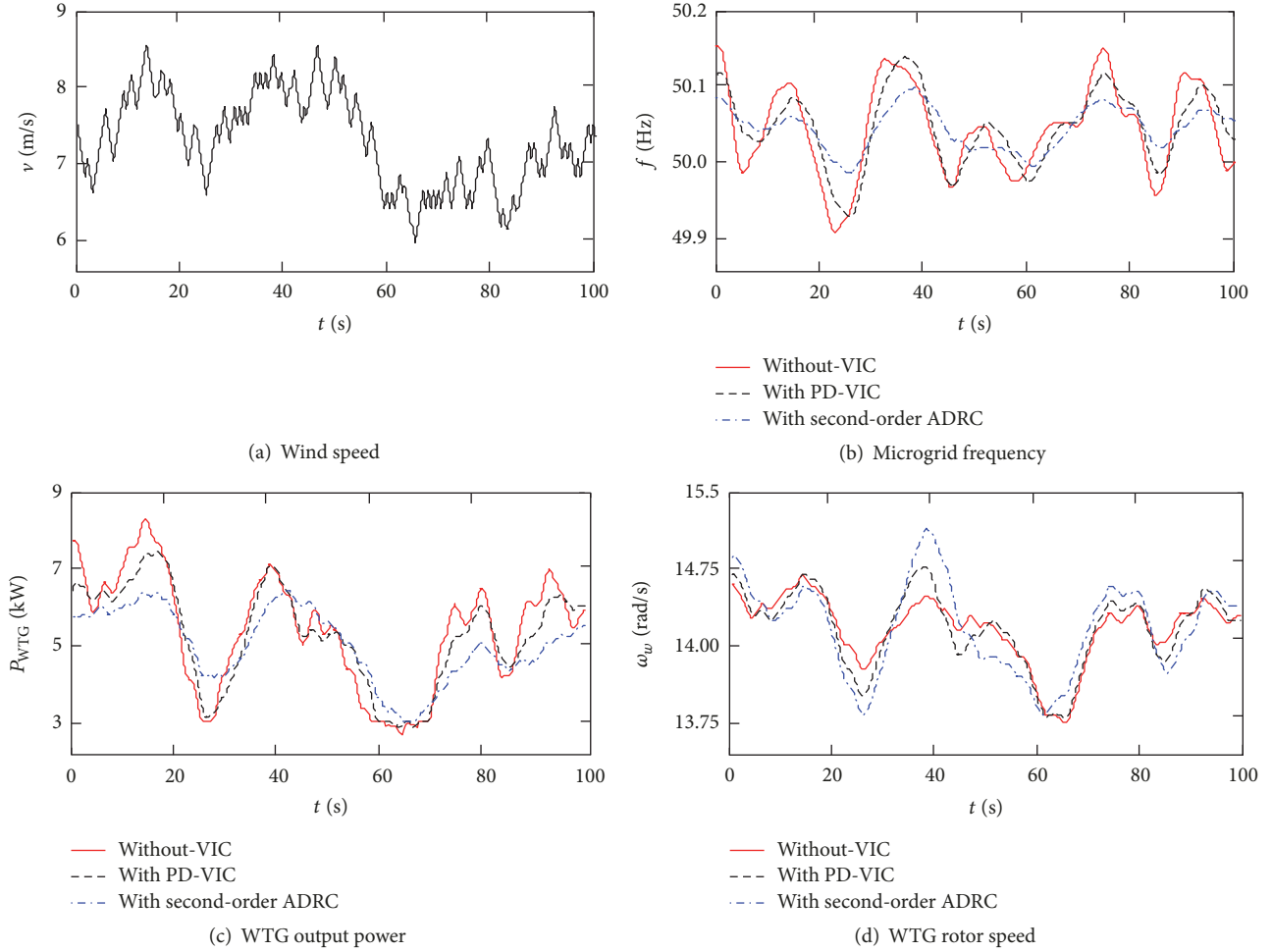


FIGURE 9: Simulation waveforms of random wind speed.

In the experimental system, the rated power of the simulative WTG is $P'_{wn} = 7.5$ kW, the rated rotor speed is $\omega'_{wn} = 18.8$ rad/s, the radius of the wind turbine is $R = 3.4$ m, and the rated wind speed is 10 m/s. The rated capacity of simulative MGT is $P'_{MGTh} = 20$ kW and inertia time constant is $T'_{CH} = 10$ s. The fixed load is $P'_{load0} = 10$ kW, and the switchable load is $P'_{load1} = 5$ kW. The controller chips of simulative WTG and MGT are DSP F2812 of TI company, the controllers exchange data with LabWindows/CVI of host computers through the RS485 communication protocol.

The design of experimental scenario: at $t = 0$, the WTG and MGT are grid-connected, $P_{WTG} = 2.5$ kW, and $P_{MGT} = 7.5$ kW. At $t = 7.5$ s, the system load was increased by 5 kW. Three groups of experiment are carried out in the order of without-VIC, PD-VIC, and ADRC-VIC. Since the focus of this paper is on the VIC algorithm of the short-time frequency regulation, the wind speed is set to a constant 6.5 m/s during this period.

5.2. The Analysis of Experimental Results. Figure 12 is the experimental waveforms of without-VIC, PD-VIC, and second-order ADRC-VIC during the load increase, respectively.

The analysis of without-VIC experimental waveforms: at $t = 7.5$ s, with sudden increase of the load P'_{load1} , the simulative MGT independently bears the load disturbance, and the fluctuation characteristic of frequency is similar to the actual MGT. As shown in Figure 12(a), the maximum frequency excursion is about $\Delta f_{max} = 1.25$ Hz, the stabilization time of frequency is about $t = 19.5$ s after three cycles of oscillation, and $\Delta t = 12$ s. In Figures 12(b) and 12(c), the output power of WTG $P_{WTG} = 2.5$ kW and the rotor speed $\omega_w = 14$ rad/s remain unchanged. In Figure 12(d), the P_{MGT} increases 5 kW by step.

The analysis of PD-VIC experimental waveforms: compared with that in without-VIC, the fluctuation amplitude of f is decreased, $\Delta f_{max} = 0.9$ Hz, the settling time is about $t = 15$ s after two cycles of oscillation, and $\Delta t = 7.5$. In Figure 12(c), the increased auxiliary power of P_{WTG} is the use of virtual inertia to participate in frequency regulation, the extreme value is $\Delta P_{VICmax} = 1.25$ kW, and P_{WTG} and ω_w have the phenomenon of oscillation and overshoot. P_{MGT} is increased 5 kW with the load increasing, but the WTG participates in the system frequency regulation with virtual inertia at this time, resulting in a distortion and overshoot phenomenon of P_{MGT} .

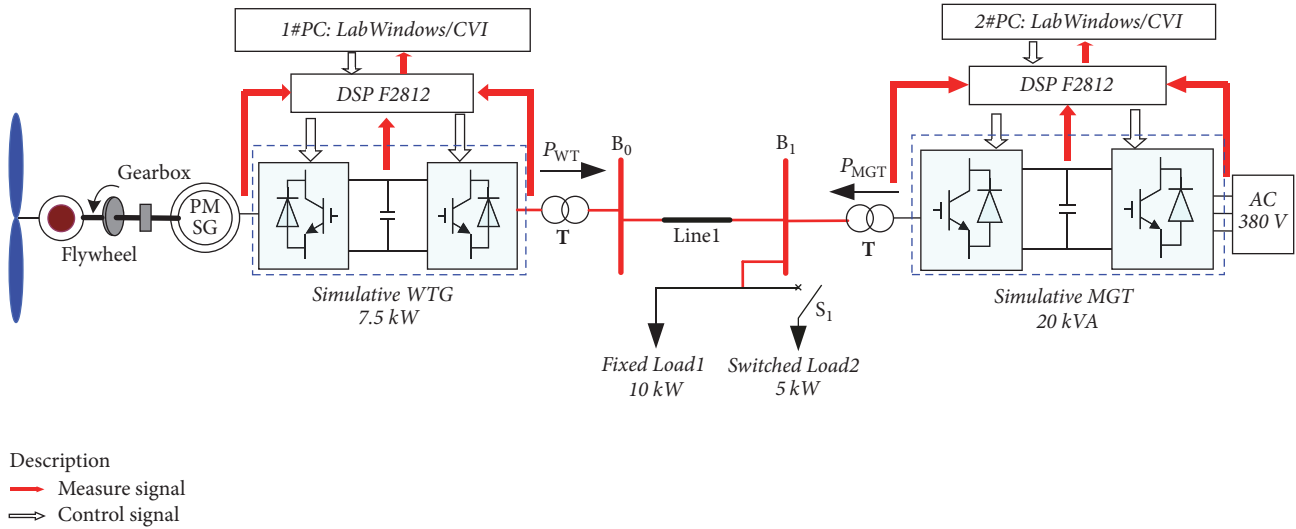


FIGURE 10: The schematic diagram of the simulative experiment system.

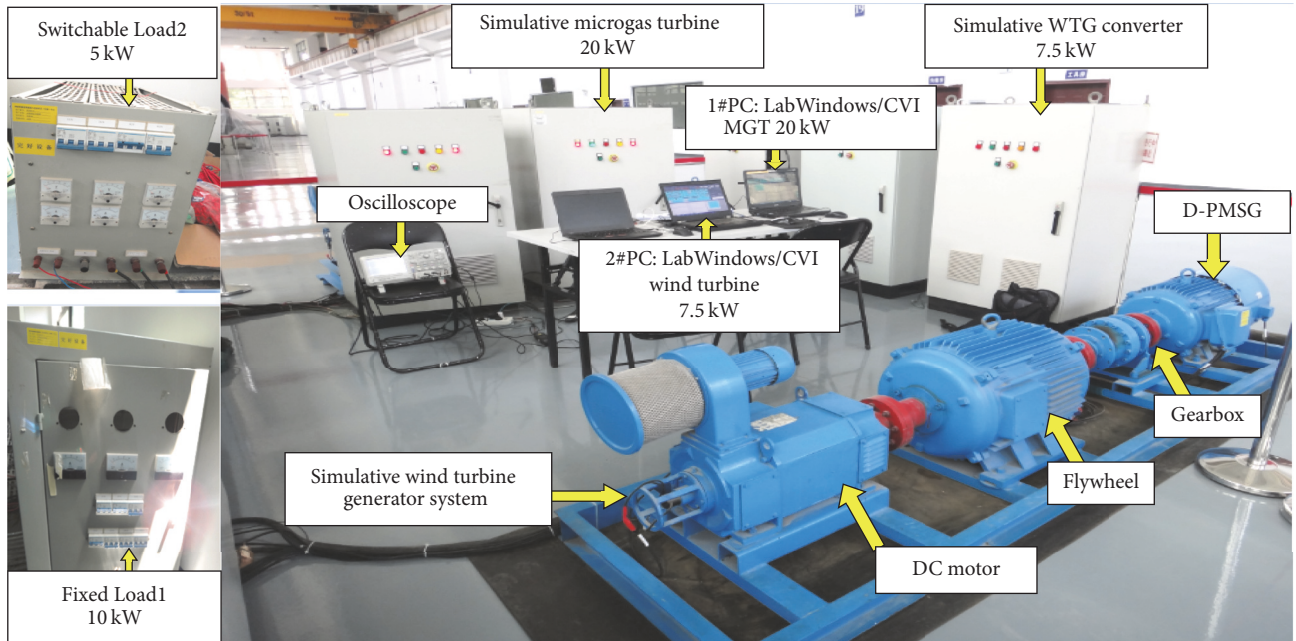


FIGURE 11: The field of the simulative experimental platform.

The analysis of second-order ADRC-VIC experimental waveforms: compared with that in without-VIC, the fluctuation amplitude of frequency is obviously reduced, the maximum deviation of the frequency is about $\Delta f_{\max} = 0.7$ Hz, the settling time is at $t = 13.5$ s or so, and $\Delta t = 5$ s. The extreme of auxiliary power is $\Delta P_{\text{VICmax}} = 2$ kW. P_{WTG} and ω_w have no phenomenon of oscillation and overshoot. Second-order ADRC-VIC makes ω_w recovery time Δt_1 longer and avoids overshoot, so that the WTG virtual inertia is released more fully. P_{MGT} appears to be no overshoot phenomenon.

Therefore, the PD-VIC and the second-order ADRC-VIC both can effectively improve the transient stability of the system frequency in the same experimental environment.

Compared with the PD-VIC, the ADRC-VIC can effectively extend the ω_w recovery time and avoid overshoot, and second-order ADRC-VIC reduces the microgrid frequency fluctuation amplitude value Δf_{\max} by 0.2 Hz, the time of stabilization Δt is reduced by about 1.5 s, and the overshoot phenomenon in P_{MGT} can be avoided.

6. Conclusions and Future Works

6.1. The Conclusions of This Paper. Based on the background of a SSM, this paper studies the algorithm of primary frequency regulation by using WTG virtual inertia and focuses on the algorithms of PD-VIC and second-order ADRC-VIC.

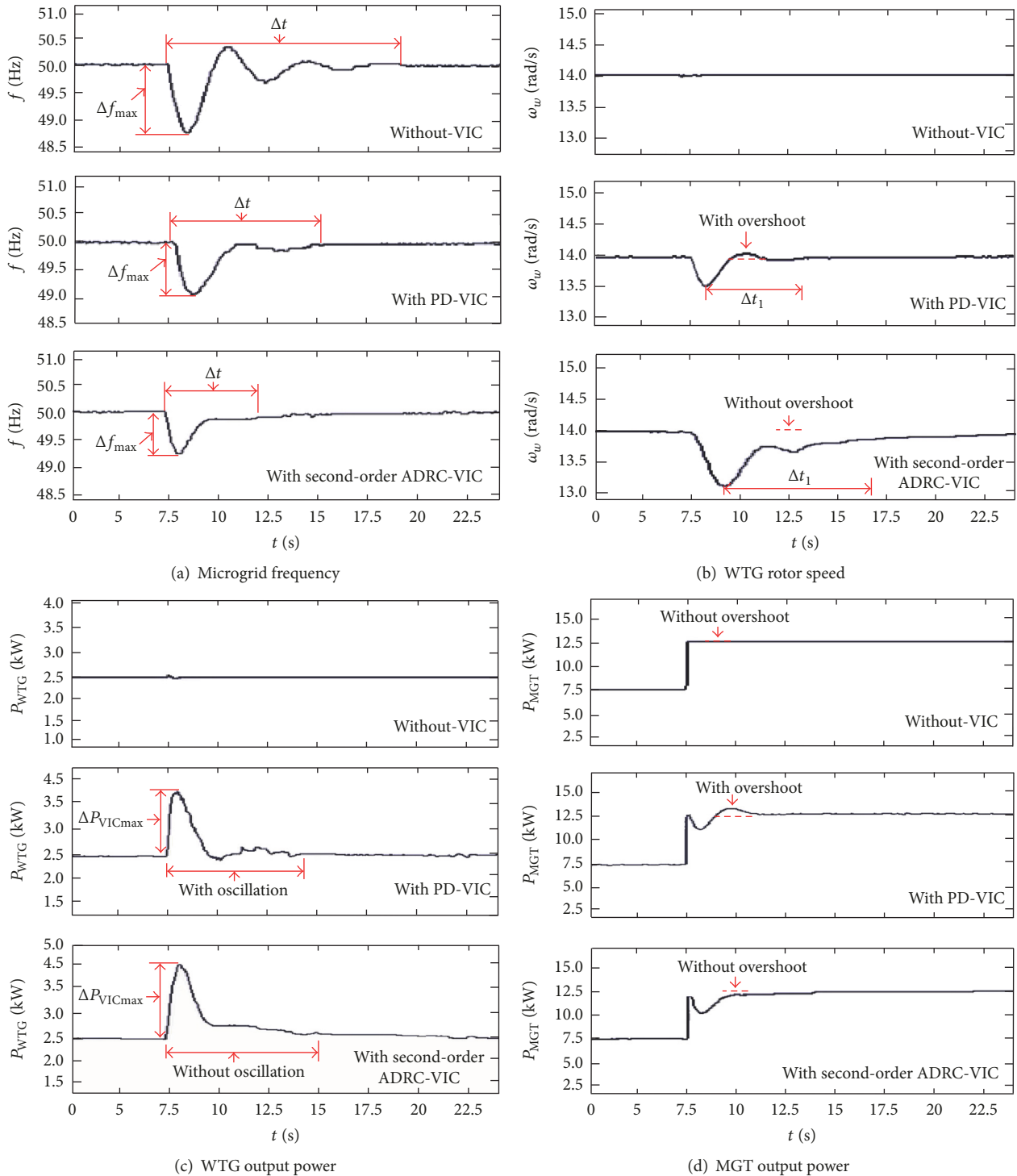


FIGURE 12: The experiment waveforms of without-VIC, PD-VIC, and second-order ADRC-VIC.

The paper shows that the PD-VIC is clear in physical meaning and easy to implement, but there is a problem that the setting of the optimal parameter is difficult and it is easy to cause overshoot. ADRC is a controller designed to suppress the system frequency disturbance. This paper presents the design and implementation of the second-order ADRC-VIC.

Through the verification of simulation and experiment, PD-VIC and second-order ADRC-VIC both can effectively use the WTG virtual inertia to participate in the system primary frequency regulation. Compared with PD-VIC, the second-order ADRC-VIC can effectively extend the ω_w recovery time and avoid overshoot, and the simulation

shows that second-order ADRC-VIC reduces the maximum deviation and the settling time of frequency by 0.15 Hz and 2 s, respectively, the experiment shows that ADRC reduces the maximum deviation and the settling time of frequency by 0.2 Hz and 1.5 s, respectively, and ADRC can avoid the overshoot of the MGT output power. Therefore, ADRC makes WTG virtual inertia release more full, and the frequency regulation effect of second-order ADRC-VIC is better.

6.2. The Future Works. This paper only studies the algorithm of the WTG virtual inertial control but does not fully consider the WTG frequency regulation capability. How to fully release the WTG virtual inertia to participate in frequency regulation is a research that needs to be done in the future. In this paper, a single WTG participating in the frequency regulation is studied only, and multiple WTGs in coordinate frequency regulation are the next research to be carried out.

Appendix

A. Parameters of Simulation Model

MGT rate power P_{MGTn} : 50 kW
 MGT inertia time constant T_{ch} : 8 s
 MGT line-to-line voltage U_n : 380 V
 a WTG rate power P_{WGTn} : 20 kW
 Microgrid steady frequency f_n : 50 Hz
 Fixed load P_{Load0} : 10 kW
 Switchable load P_{Load1} : 5 kW
 PD coefficients k_{pf} , k_{df} : 2×10^3 , 1.5×10^3
 Sampling step size h : 0.001 s
 ESO parameters β_1 , β_2 , and β_3 : 1000, 334, and 332
 ESO parameters a_1 , a_2 , δ , and b : 0.5, 0.8, 1, and 1/24
 NLSFE parameters β_{01} , β_{02} : 70, 10
 NLSFE parameters a_{01} , a_{02} , δ_0 , and a : 0.5, 2, 1, and 24

B. Parameters of Experimental System

MGT rate power P'_{MGTn} : 20 kW
 MGT inertia time constant T'_{ch} : 10 s
 MGT line-to-line voltage U'_n : 380 V
 a WTG rate power P'_{MGTn} : 7.5 kW
 Fixed load P'_{load0} : 10 kW
 Switchable load P'_{load1} : 5 kW
 PD coefficients k'_{pf} , k'_{df} : 1.2×10^3 , 1.1×10^3
 Sampling step size h' : 0.01 s
 ESO parameters β'_1 , β'_2 , and β'_3 : 100, 34, and 31
 ESO parameters a'_1 , a'_2 , δ' , and b' : 0.7, 0.9, 1, and 1/40
 NLSFE parameters β'_{01} , β'_{02} : 90, 30
 NLSFE parameters a'_{01} , a'_{02} , δ'_0 , and a' : 0.7, 5, 3, and 40

Conflicts of Interest

The authors declare that there are no conflicts of interest regarding the publication of this article.

Acknowledgments

This work is supported by the National Natural Science Foundation of China (Grant no. 51377167) and the National Basic Research Program (973 Program) of China (2012GB215103).

References

- [1] N. Bizon, "Load-following mode control of a standalone renewable/fuel cell hybrid power source," *Energy Conversion and Management*, vol. 77, pp. 763–772, 2014.
- [2] E. Rakhshani and J. Sadeh, "Practical viewpoints on load frequency control problem in a deregulated power system," *Energy Conversion and Management*, vol. 51, no. 6, pp. 1148–1156, 2010.
- [3] H. Bevrani, F. Habibi, P. Babahajyani, M. Watanabe, and Y. Mitani, "Intelligent frequency control in an AC microgrid: Online PSO-based fuzzy tuning approach," *IEEE Transactions on Smart Grid*, vol. 3, no. 4, pp. 1935–1944, 2012.
- [4] F. Khater and A. Omar, "A Review of Direct Driven PMSG for Wind Energy Systems," *Journal of Energy and Power Engineering*, vol. 7, pp. 1592–1603, 2013.
- [5] F. Sircilli, S. J. P. Retief, L. B. Magalhães et al., "Measurements of a micro gas turbine plume and data reduction for the purpose of infrared signature modeling," *IEEE Transactions on Aerospace and Electronic Systems*, vol. 51, no. 4, pp. 3282–3293, 2015.
- [6] T. S. Bhatti, A. A. F. Al-Ademi, and N. K. Bansal, "Load frequency control of isolated wind diesel hybrid power systems," *Energy Conversion and Management*, vol. 38, no. 9, pp. 829–837, 1997.
- [7] F. Díaz-González, M. Hau, A. Sumper, and O. Gomis-Bellmunt, "Coordinated operation of wind turbines and flywheel storage for primary frequency control support," *International Journal of Electrical Power & Energy Systems*, vol. 68, pp. 313–326, 2015.
- [8] W. Tan, "Decentralized load frequency controller analysis and tuning for multi-area power systems," *Energy Conversion and Management*, vol. 52, no. 5, pp. 2015–2023, 2011.
- [9] T. Malakar, S. K. Goswami, and A. K. Sinha, "Impact of load management on the energy management strategy of a wind-short hydro hybrid system in frequency based pricing," *Energy Conversion and Management*, vol. 79, pp. 200–212, 2014.
- [10] U. N. Rahmat, T. Thiringer, and D. Karlsson, "Temporary primary frequency control support by variable speed wind turbines potential and applications. IEEE Trans. Power Syst," in *IEEE Trans. Power Syst*, vol. 23, pp. 601–612, 2008.
- [11] J. Morren, S. W. H. de Haan, W. L. Kling, and J. A. Ferreira, "Wind turbines emulating inertia and supporting primary frequency control," *IEEE Transactions on Power Systems*, vol. 21, no. 1, pp. 433–434, 2006.
- [12] N. Rezaei and M. Kalantar, "Smart microgrid hierarchical frequency control ancillary service provision based on virtual inertia concept: An integrated demand response and droop controlled distributed generation framework," *Energy Conversion and Management*, vol. 92, pp. 287–301, 2015.
- [13] K. V. Vidyandandan and N. Senroy, "Primary frequency regulation by deloaded wind turbines using variable droop," *IEEE Transactions on Power Systems*, vol. 28, no. 2, pp. 837–846, 2013.

- [14] M. Akbari and S. M. Madani, "Analytical evaluation of control strategies for participation of doubly fed induction generator-based wind farms in power system short-term frequency regulation," *IET Renewable Power Generation*, vol. 8, no. 3, pp. 324–333, 2014.
- [15] R. Ponciroli, A. Cammi, S. Lorenzi, and L. Luzzi, "Control approach to the load frequency regulation of a Generation IV Lead-cooled Fast Reactor," *Energy Conversion and Management*, vol. 103, pp. 43–56, 2015.
- [16] V. Ravikumar Pandi, A. Al-Hinai, and A. Feliachi, "Coordinated control of distributed energy resources to support load frequency control," *Energy Conversion and Management*, vol. 105, pp. 918–928, 2015.
- [17] M. Shiroei and A. M. Ranjbar, "Supervisory predictive control of power system load frequency control," *International Journal of Electrical Power & Energy Systems*, vol. 61, pp. 70–80, 2014.
- [18] Y. Tang, Y. Bai, C. Huang, and B. Du, "Linear active disturbance rejection-based load frequency control concerning high penetration of wind energy," *Energy Conversion and Management*, vol. 95, pp. 259–271, 2015.
- [19] A. Boukhriss, A. Essadki, A. Bouallouch, and T. Nasser, "Maximization of generated power from wind energy conversion systems using a doubly fed induction generator with active disturbance rejection control," in *Proceedings of the 2nd World Conference on Complex Systems, WCCS 2014*, pp. 330–335, November 2014.
- [20] A. Boukhriss, T. Nasser, and A. Essadki, "A linear active disturbance rejection control applied for DFIG based wind energy conversion system," *Int J Comput Sci Iss*, vol. 10, pp. 391–399, 2013.
- [21] F. Akel, T. Ghennam, E. M. Berkouk, and M. Laour, "An improved sensorless decoupled power control scheme of grid connected variable speed wind turbine generator," *Energy Conversion and Management*, vol. 78, pp. 584–594, 2014.
- [22] J. Q. Han, "From PID to active disturbance rejection control," *IEEE Transactions on Industrial Electronics*, vol. 56, no. 3, pp. 900–906, 2009.
- [23] D. Sun, "Comments on active disturbance rejection control," *IEEE Transactions on Industrial Electronics*, vol. 54, no. 6, pp. 3428–3429, 2007.
- [24] C.-Z. Huang and Q. Zheng, "Frequency response analysis of linear active disturbance rejection control," *Sensors and Transducers*, vol. 157, no. 10, pp. 346–354, 2013.
- [25] B.-Z. Guo and Z.-L. Zhao, "On convergence of non-linear extended state observer for multi-input multi-output systems with uncertainty," *IET Control Theory & Applications*, vol. 6, no. 15, pp. 2375–2386, 2012.
- [26] R. Yang, M. Sun, and Z. Chen, "Active disturbance rejection control on first-order plant," *Journal of Systems Engineering and Electronics*, vol. 22, no. 1, pp. 95–102, 2011.
- [27] H. Bevrani, T. Ise, and Y. Miura, "Virtual synchronous generators: A survey and new perspectives," *International Journal of Electrical Power and Energy Systems*, vol. 54, pp. 244–254, 2014.

